frontiers in Nanotechnology

ORIGINAL RESEARCH
published: 27 April 2021
doi: 10.3389/fnano.2021.670762

Engineering Method for Tailoring Electrical Characteristics in TiN/TiO_x/HfO_x/Au Bi-Layer Oxide Memristive Devices

Seongae Park[1,2]*, *Stefan Klett*[1], *Tzvetan Ivanov*[1,2], *Andrea Knauer*[2], *Joachim Doell*[2] and *Martin Ziegler*[1,2]*

[1]Department of Electrical Engineering and Information Technology, Technische Universtität Ilmenau, Ilmenau, Germany, [2]Institute of Micro and Nanotechnologies MacroNano, Technische Universtität Ilmenau, Ilmenau, Germany

OPEN ACCESS

Edited by:
Huanglong Li,
Tsinghua University, China

Reviewed by:
Guangdong Zhou,
Southwest University, China
Dashan Shang,
Institute of Microelectronics, China

***Correspondence:**
Seongae Park
seongae.park@tu-ilmenau.de
Martin Ziegler
martin.ziegler@tu-ilmenau.de

Specialty section:
This article was submitted to Nanodevices, a section of the journal Frontiers in Nanotechnology

Received: 22 February 2021
Accepted: 26 March 2021
Published: 27 April 2021

Citation:
Park S, Klett S, Ivanov T, Knauer A, Doell J and Ziegler M (2021) Engineering Method for Tailoring Electrical Characteristics in TiN/TiO_x/HfO_x/Au Bi-Layer Oxide Memristive Devices. Front. Nanotechnol. 3:670762. doi: 10.3389/fnano.2021.670762

Memristive devices have led to an increased interest in neuromorphic systems. However, different device requirements are needed for the multitude of computation schemes used there. While linear and time-independent conductance modulation is required for machine learning, non-linear and time-dependent properties are necessary for neurobiologically realistic learning schemes. In this context, an adaptation of the resistance switching characteristic is necessary with regard to the desired application. Recently, bi-layer oxide memristive systems have proven to be a suitable device structure for this purpose, as they combine the possibility of a tailored memristive characteristic with low power consumption and uniformity of the device performance. However, this requires technological solutions that allow for precise adjustment of layer thicknesses, defect densities in the oxide layers, and suitable area sizes of the active part of the devices. For this purpose, we have investigated the bi-layer oxide system TiN/TiO_x/HfO_x/Au with respect to tailored I-V non-linearity, the number of resistance states, electroforming, and operating voltages. Therefore, a 4-inch full device wafer process was used. This process allows a systematic investigation, i.e., the variation of physical device parameters across the wafer as well as a statistical evaluation of the electrical properties with regard to the variability from device to device and from cycle to cycle. For the investigation, the thickness of the HfO_x layer was varied between 2 and 8 nm, and the size of the active area of devices was changed between 100 and 2,500 μm^2. Furthermore, the influence of the HfO_x deposition condition was investigated, which influences the conduction mechanisms from a volume-based, filamentary to an interface-based resistive switching mechanism. Our experimental results are supported by numerical simulations that show the contribution of the HfO_x film in the bi-layer memristive system and guide the development of a targeting device.

Keywords: memristive devices, neuromorphic systems, bi-layer oxide memristive devices, memristive layer engineering, numerical simulation

1 INTRODUCTION

Memristive devices have been under the spotlight as an ideal element for neuromorphic computing due to their outstanding characteristics to emulate bio realistic information processing (Versace and Chandler, 2010; Legenstein, 2015; Mohammad et al., 2016; Jeong and Shi, 2019; Krestinskaya et al., 2020). Their non-volatile memory property, which is induced by an adaptation of the resistance state by applying electrical signals, makes them ideal candidates for the emulation of synaptic functionalities in artificial neural networks (Sah et al., 2014). For this application, they enable the realization of extremely energy-efficient hardware (Massimiliano and Yuriy, 2013; Ignatov et al., 2017) and have the potential of a high integration capability due to their simple two-terminal device structure (Lin et al., 2020). In particular, the integration of memristive devices in crossbar structures is worthy of mentioning here, which makes it possible to implement efficient learning schemes (Prezioso et al., 2015; del Valle et al., 2018; Alibart et al., 2013).

When considering the wide range of different neuromorphic systems, two main fields of applications in neuromorphic systems can be distinguished (Ielmini and Ambrogio, 2020): (i) neurobiologically realistic learning schemes and (ii) machine learning based algorithms. In neurobiologically realistic learning schemes the synaptic connections of a network are tuned by time-encoded spike-like signals (Snider, 2008), which typically requires nonlinear memristive device characteristics in a time-dependent manner (Ziegler et al., 2015; Dittmann and Strachan, 2019). In contrast to that, machine learning based algorithms use vector-matrix multiplications in which an explicit time dependence is not required (Ziegler et al., 2018). For that application, it is more important to set very precisely different resistance values for the individual memristive cells in a crossbar array (Yakopcic et al., 2015). Therefore, a time-independent linear resistance modulation is desirable (Chandrasekaran et al., 2019) which requires a high symmetry between the setting and the resetting characteristic of the memristive device over a wide range of resistance states (Wang et al., 2016).

In last couple of years many memristive device structures have been presented that are adequate for the machine learning algorithms (Kim et al., 2017; Cüppers et al., 2019; Li et al., 2020; Yao et al., 2020). It has been shown that the use of the memristive devices can significantly simplify the training routine in massively interconnected networks (Wang et al., 2019). Among those devices, particularly, memristive devices with a metal oxide bi-layer structure gained considerable interest in that field. Those memristive devices showed a significant improvement in the resistance modulation linearity (Li et al., 2018a) and the number of resistance states (Stathopoulos et al., 2017) along with the reduced variability in the resistive switching characteristics (Wang et al., 2010). The bi-layer metal oxide devices typically consist of an oxide layer that serves as a reservoir of oxygen vacancies and a solid state electrolyte layer which builds a Schottky-like interface contact with the adjacent metallic electrode (Huang et al., 2012; Bousoulas et al., 2016; Kim et al., 2018; Xiong et al., 2019). The resistive switching mechanism can be described as follows (Cüppers et al., 2019): under an external bias voltage oxygen vacancies are injected from the reservoir layer into the solid state electrolyte layer in which the oxygen vacancies are forming a filamentary conduction path toward the metallic electrode. This reduces both the resistance of the electrolyte layer and the Schottky barrier height and leads to a lowering of the overall device resistance (Asanuma et al., 2009; Zhao et al., 2020). An alternative concept of a memristive bi-layer metal oxide device is the double barrier memristive devices (DBMD) (Hansen et al., 2015). In this device structure, an ultra-thin solid electrolyte layer is sandwiched between a metal oxide layer and a metal electrode forming a Schottky-like contact. Here, the metal oxide layer serves as a diffusion barrier for oxygen ions, but not as a reservoir (Hur et al., 2010; Yin et al., 2015; Clima et al., 2016; Dirkmann et al., 2016; Hansen et al., 2017). The resistive switching effect is based on a shift of the oxygen ions in the solid state electrolyte layer in the direction of the metal electrode, which also leads to a reduction of the Schottky barrier height (Dirkmann et al., 2016). The advantage of the non-filamentary type of devices is that they did not require an electroforming step (Yoon et al., 2014), and the switching effect is based on a defined interface effect (Govoreanu et al., 2013). However, a disadvantage compared to bi-layer metal oxide devices with oxygen vacancy filaments is the shorter retention time (Solan et al., 2017). Furthermore, DBMDs have a rectifying characteristic (Gao et al., 2015) and thus a high asymmetry in the voltage polarity. However, these devices allow the realization of selector-free crossbar structures (Ma et al., 2017; Hansen et al. 2018) and the realization of biologically realistic computational schemes (Wang et al., 2015; Diederich et al., 2018).

A common challenge in the development of memristive devices is a tailor-made design of memristive devices for a respective computational scheme (Pei et al., 2015). For this, a number of materials and technology parameters have to be considered, such as the concentration of oxygen vacancies (He et al., 2017) or active ions (Clima et al., 2016), materials for the active layers and interface (connecting) layers (Li et al., 2018b). But also geometrical parameters such as layer thicknesses (Park et al., 2015; Wang et al., 2016; Li et al., 2018a) and size of the active areas (Lee et al., 2010) have to be considered carefully. These parameters are often only slightly known or not known at all but must be related to the device performance for a reliable device functionality (Niu et al., 2010; Lee et al., 2011). This particularly requires systematic investigations of the individual parameters and suitable device technology combined with a profound understanding of the underlying physical processes (Sun et al., 2019).

The aim of this work is to bridge the gap between the material design and the electronic characteristics of memristive devices for a tailored development of bi-layer metal oxide devices for neuromorphic systems. For this purpose, the bi-layer system $TiN/TiO_x/HfO_x/Au$ is examined in more detail in this paper. In detail, a four-inch wafer technology is presented, which allows to vary different device parameters, such as layer thickness and area size of the devices over the wafer. Using automated electronic measurements, a statistic of important device characteristics is

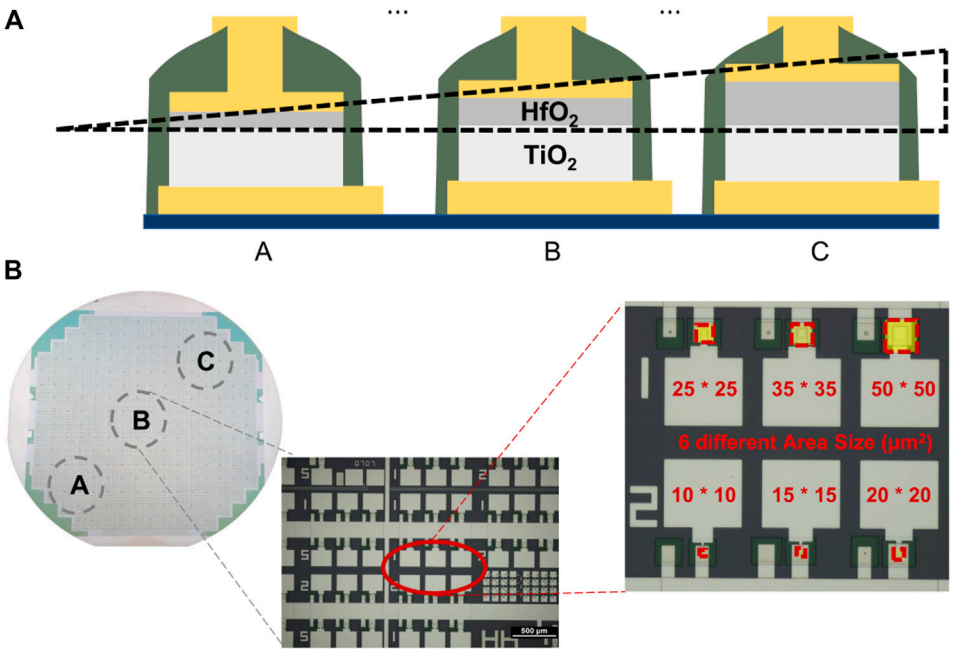

FIGURE 1 | Schematic representation of the technology for bi-layer oxide memristive devices: Using different sputtering geometries (referred to as methods 1 and 2 in the text), different types of devices have been produced, showing filamentary switching (referred to as type F) and area-based resistance switching (referred to as type R). **(A)** Cross-section of TiN/TiO_x/HfO_x/Au bi-layer oxide memristive devices over the wafer. The used deposition method (method 2) allows for a variation of the thickness of HfO_x layer from 2 to 8 nm. **(B)** Microscope images of a complete 4-inch wafer with 40,000 single devices and sections, showing the individual cells which consist of clusters with six devices, each with a different area size. Three regions on the wafer are indicated as A, B, and C. Each region has an area size of 0.5 × 0.5 cm^2. For type R devices a 2 nm HfO_x was deposited on all the three regions, while the thicknesses for type F have 2, 5, and 8 nm HfO_x films on region A, B, and C, respectively. Here, it was assumed that the HfO_x thickness is the same in each region due to the 1-dimensional thickness change over a 4-inch wafer and the relatively small area size. Approximately 60 memristive devices were measured in each area A, B, and C, respectively, for type F.

collected, and related to material properties and technology parameters. For a detailed understanding of the resistive switching mechanism, a physical device model is presented, which also allows a detailed examination of the individual device parameters. Essentially, we show that different sputtering conditions can influence oxygen ion and oxygen vacancy concentrations in the HfO_x layer. This causes different device characteristics. While an area-based switching mechanism leads to a rectifying current-voltage characteristic at high layer qualities with few oxygen vacancies, filamentary structures are formed in the HfO_x layer at higher concentrations of oxygen vacancies. This leads to a symmetrical current-voltage characteristic with multilevel resistant states and improved retention. In both cases, a change in the Schottky barrier between the HfO_x layer and the Au electrode can be identified as the reason for the observed switching effect. For a tailored design of memristive devices for their application, the different electronic characteristics are related to possible applications in neuromorphic systems.

The present work is structured as follows: In chapter 2, the implemented technology for manufacturing the memristive devices is presented first. Then the used methods for material and electrical characterization of the devices are discussed. Finally, chapter 2 presents a physical device model that serves to describe the underlying physical effects of the resistive switching mechanisms. In chapter 3, the obtained results are presented and discussed. For this purpose, first, the results of the electrical measurements and their statistics are shown in relation to an individual device and technology parameters. Then, important parameters of the devices are related to their electronic characteristics using the simulation model. Finally, the chapter discusses the application of the devices in neuromorphic computing architectures. The presented results are summarized in chapter 4.

2 MATERIALS AND METHODS

2.1 Device Technology

Figure 1 shows a developed device technology for bi-layer oxide memristive devices. In **Figure 1A** cross-sections of the fabricated TiN(50 nm)/TiO_x (30 nm)/HfO_x (2–8 nm)/Au(50 nm) bi-layer memristive devices with Al(300 nm) contact pads are sketched. They are fabricated on a 4-inch oxidized silicon wafer (1 µm of thermal SiO_x) in the full device technology. This technology is overviewed in **Figure 1B** and contains around 40,000 single devices, including test structures for the device development (see microscope images in **Figure 1B**). This allows the investigation of various device parameters, such as the active device area (six different area sizes are realized, as shown in **Figure 1B**), the thickness of the active HfO_x layer, and the material compositions over the wafer for a targeted

development of memristive devices. For a variation of the latter parameter, two different sputtering methods for the HfO_x layer were used. In particular, a variation in oxygen vacancies is required to achieve a desired resistive switching process in this class of memristive devices (He et al., 2017). Here, using a sputtering system equipped with three confocal source targets, two methods are employed for the deposition of the HfO_x which are referred to as method 1 and 2. During the deposition, the substrate is rotated to obtain a uniform film thickness, while a wedge film is formed without a rotation. The wedge is formed only along one direction. For method 1 the HfO_x layer was deposited on the wafer under optimal conditions, i.e., rotation of the substrate within a confocal sputtering arrangement. For method 2 the wafer was not rotated during the sputtering of the HfO_x layer. This leads to a reduced layer quality, but also a wedge over the wafer as shown in **Figure 1A** (further details are discussed below). As a result, we obtained two distinctive bi-layer oxide memristive device structures, which are referred to in the following as device R and device F.

In more detail, the TiO_x/HfO_x bi-layer was deposited on an inertial reactive sputtered TiN bottom-electrode via DC magnetron sputtering, where O_2/Ar of reactive gas was adjusted with the ratio of 10/40 and 10/29 for the TiO_x and HfO_x film, respectively. After the TiO_x was sputtered, the thickness of the HfO_x was controlled using the two discussed sputtering methods 1 (for device type R) and 2 (for device type F): as seen in **Figure 1A** a wedge layer with a variation of the HfO_x thickness from 2 to 8 nm was obtained for device F, where devices were fabricated along the axis (x-direction) perpendicular to the axis of the wedge (y-direction). Device R has a 2 nm uniform HfO_x layer. The layer deposition was finalized with an Au top-electrode layer. Thereafter, the material stack was patterned using photolithography and reactive ion etching for device R, while a lift-off in Dimethylsulfoxide (DMSO) was used for device F. The lift-off process was carried out due to the thickness variation of HfO_x in device F. Here, the investigation of the switching behaviors was preceded after we confirmed that the two patterning methods scarcely affected electrical characteristics. All devices were insulated with SiO_2 layers from the ambient air to avoid the influence of moisture in switching behaviors (Tsuruoka et al., 2012; Zhou et al., 2018; Zhou et al., 2020) (**Figure 1A**), and Al contact pads were deposited by e-beam evaporation.

2.2 Material Characterization

The development of the memristive devices was supported by a material characterization accompanying the manufacturing process. The thickness and the composition of the layers were characterized by ellipsometry measurements (SE500, Sentech) and surface profile measurements (Dektak 150, Veeco).

For a detailed material investigation, unstructured HfO_x films were deposited on silicon substrates. Therefore, the two described sputtering methods 1 and 2 were employed to deposit 37 nm thick HfO_x films. On those films ellipsometry measurements were performed at 632.8 nm at 70° of incidence. As the results, refractive indices of $n = 1.9889$ and $n = 2.0285$ were measured for, respectively, the uniform (method 1) and the wedge- (method 2) deposited HfO_x films. Thus, in agreement with previous investigations (Martínez et al., 2007) the film can be assumed to have amorphous crystallinities. However, the obtained n value from the uniform deposited film was higher than n of the wedge deposited HfO_2 film, which can be attributed to a reduced packing density (Gao et al., 2016).

Furthermore, X-ray photoelectron spectroscopy (XPS) measurement was utilized to study the quantitative atomic ratio O/Hf in sputtered HfO_x layers. The XPS analysis were carried out using monochromatic Al_K-alpha radiation (excitation energy hν = 1,486.68 eV) under charge neutralization using a SPECS SAGE HR 150 XPS system equipped with a 1D delayline detector and a Phoibos 150 analyzer. The calibration of the energy scale was ensured by reference measurements on a polycrystalline silver sample. Before the measurements, HfO_x was sputtered on Si/SiO_2 wafers for 900 s using the two different sputtering method 1 and 2. As a result, a ratio of O/Hf of 1.80/1 was observed for deposition method 2, while a ratio of 1.98/1 was recorded for samples sputtered via method 1 (see **Supplementary Data S1**). The sputtering method 1 provides a stoichiometry close to HfO_2, while the obtained stoichiometry via method 2 leads to optimal condition for the forming of oxygen vacancy filaments (McKenna, 2014). Thus, we can conclude that sputtering method 1 leads to a reduced number of oxygen vacancies than the sputtering method 2. Hence, a HfO_x layer with a higher density of oxygen vacancies can be assumed for device type F in respect to device type R.

2.3 Electrical Characterization

Current-voltage measurements (I-V curves) and voltage pulse measurements were carried out to characterize the electrical properties of TiO_x/HfO_x bi-layer memrsitive devices using a source measurement unit (Keysight b2901a). Therefore, a voltage is applied to the top-electrode of the device (bottom-electrode were grounded), while the current has been measured simultaneously. Furthermore, current compliance was imposed during the measurement to prevent the device from damage. The used current compliance was $I_{CC} = 10\,\mu A$, $I_{CC} = -5\,mA$ for R and F devices, respectively. For pulse measurements the device resistance was measured at, respectively, 1 and 0.1 V for R and F devices. The switching voltage to set and reset the device resistances was 3 V/−2 V for device type R and −1 V/1.5 V for F type devices. For both devices a pulse duration of ~10 ms was used. For a statistical evaluation of the electrical properties, median values were extracted taking into account the variability in cycle to cycle (C2C), and device to device (D2D). In the C2C investigation 10 times of DC voltage sweep cycles in one device were carried out. For reliable statistics, automated measurements of more than 10 memristive devices in each device parameter were performed, which means a total of 180 devices measured for three different thicknesses and six different area sizes. Both C2C and D2D statistics were investigated in DC conditions.

2.4 Physics Based Device Model

For a profound understanding of the resistive switching mechanisms and a targeted development of the devices a physics based device model was developed. In **Figure 2A** a sketch of this device model is shown: the model consists of

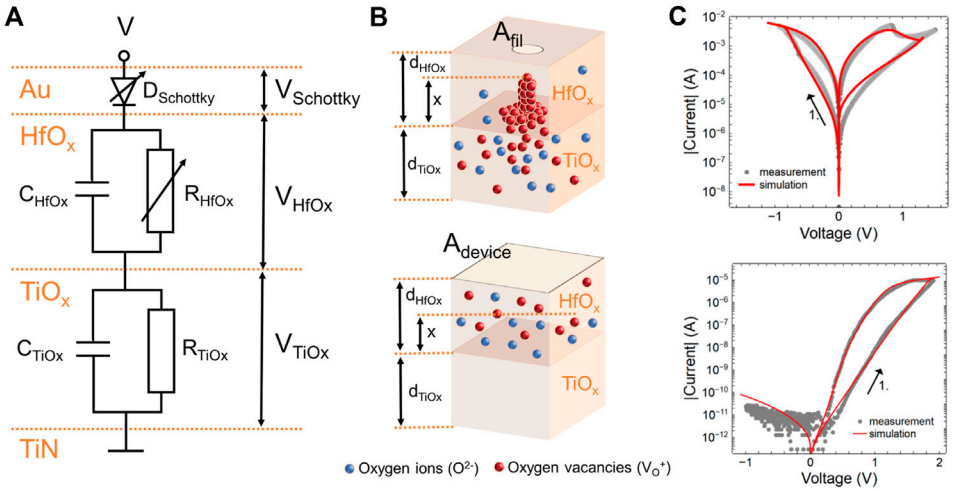

FIGURE 2 | (A) Sketch of the physics based device model for TiN/TiO_x/HfO_x/Au memristive devices. The model consists of two RC elements in the TiO_x and HfO_x layers and a Schottky diode at the interface of HfO_x and Au top-electrode. The external source voltage is divided into three local voltage drops at the HfO_x, TiO_x layers, and the Schottky diode. **(B)** Two different resistive switching mechanisms of type F devices **(top)** and type R devices **(bottom)** are considered. While in type F devices oxygen vacancies form a filamentary conductive path in the HfO_x film under an external voltage, in type R devices oxygen ions in the HfO_x film drift toward the top metal-electrode. As a result, in both device types the changed ion concentration leads to a modulation of the Schottky barrier height, which leads to the switching behaviors. Hereby originates the difference in the switching mechanisms from the density of the oxygen vacancies in the HfO_x film. **(C)** Measured I-V curves (gray) and the simulation results (red) for type F **(top)** and type R **(bottom)** devices. The arrows point to the SET direction.

two RC elements representing, respectively, the HfO_x and the TiO_x layer. The metal-semiconductor contact between the HfO_x layer and the Au electrode is considered by a Schottky diode ($D_{Schottky}$). Thus, an external applied voltage (V) is divided into the local voltage drops at the Schottky diode ($V_{Schottky}$), over the HfO_x layer (V_{HfOx}) and the TiO_x layer (V_{TiOx}) according to

$$V = V_{Schottky} + V_{HfOx} + V_{TiOx} \tag{1}$$

An important difference between here investigated two types of memristive devices is sketched in **Figure 2B**. While for the type F device a filament of oxygen vacancies is formed under the external voltage application, the type R device does not form any filaments. Essential for this is the concentration of oxygen ions and vacancies in the active HfO_x layer (Dirkmann et al., 2018). For the filamentary device F, we assumed that a number of oxygen vacancies are the mobile ions that vary between a minimum and a maximum concentration, denoted as N_{min} and N_{max}, respectively. In detail, for the filamentary device F we estimated $N_{min} = 4 \cdot 10^{24}\, m^{-3}$ and $N_{max} = 2 \cdot 10^{27}\, m^{-3}$ in accordance with the previous work (Menzel et al., 2011; Dirkmann et al., 2018). On the other hand, for the device type R we assumed a significantly lower concentration of oxygen vacancies due to a better layer quality. Here, the mobile species are oxygen ions where a concentration of $N = 10^{23}\, m^{-3}$ was used which is in qualitative agreement with (Dirkmann et al., 2016).

The concentration of the oxygen ions and vacancies has a particular effect on the active area used for resistance switching (cf. **Figure 2B**). Thus, for the filamentary device F only the filament area is relevant for the switching effect, i.e., $A = A_{fil}$ (see upper drawing in **Figure 2B**). For the type R device the whole device area is involved in the switching mechanism, i.e., $A = A_{device}$ (see lower drawing in **Figure 2B**). Both, the active area and the oxygen ion/vacancy concentration, are relevant for the resistance of the HfO_x layer:

$$R_{HfOx} = \frac{d_{HfOx}}{e \cdot zv_0 \cdot A \cdot \mu_n \cdot N} \tag{2}$$

where μ_n is the electron mobility, zv_0 is the ion charge number, and e is the elementary charge (Hardtdegen et al., 2018).

The layer thickness of TiO_x is significantly larger than that of HfO_x. Therefore, a much lower local electrical field strength is assumed ($E = V_{layer}/d_{layer}$). Thus, under an external bias voltage oxygen ion drift is suppressed within the TiO_x layer and the resistance R_{TiOx} of the TiO_x layer can be assumed to be constant. Nevertheless, the TiO_x layer plays a crucial role in the functionality of the bi-layer oxide structure: (i) it serves as a reservoir for oxygen vacancies in filament devices, and (ii) it stabilizes the switching process for both types of devices (Stathopoulos et al., 2017; Hardtdegen et al., 2018; Mikhaylov et al., 2020). For the latter point, the electronic contribution of the TiO_x layer is particularly important and has to be captured in the model. In general, the electronic charge transport through metal oxide layers can be determined by various transport mechanisms. It has been shown that a good approximation for the electron current is given by the following voltage realization (Jiang et al., 2016):

$$I_{TiOx} = j_0 \cdot A \cdot sinh(V_{TiOx}) \tag{3}$$

where j_0 is a fit parameter that has to be adapted to the real devices. The layer capacitances are given by

$$C_{layer} = \varepsilon \frac{A}{d_{layer}} \tag{4}$$

where $\varepsilon = \varepsilon_r \varepsilon_0$ is the permittivity of the respective layer.

The starting point of the switching model is the memristive behavior caused by a temporal and spatial change of the oxygen ions in the HfO_x layer. This effect is taken into account in the device model via an average ion velocity.

$$\frac{dx}{dt} = c_{drift} \cdot I_{Ion} \tag{5}$$

where x is the memristive state variable, i.e., the average position of oxygen ions or length of the filament in the HfO_x layer (cf. **Figure 2B**) and I_{Ion} is the ionic current of the oxygen ions. Furthermore, c_{drift} describes the resulting drift constant of the system, which is defined as

$$c_{drift} = \frac{\mu_n \cdot R_{mean}}{d_{HfOx} \cdot A} \tag{6}$$

Here, R_{mean} is the mean resistance of the HfO_x layer, which is given by $R_{mean} = \frac{1}{2} \cdot [R_{min} + R_{max}]$ for devices of type F and $R_{mean} = R_{HfOx}$ for the devices of type R. In particular, for devices of type F the resistance of the HfO_x layer can be specified as a function of the memristive state variable x:

$$R_{HfOx} = \frac{d_{HfOx}}{e \cdot z\nu_0 \cdot A \cdot \mu_n} \cdot \left[\frac{1}{N_{max}} \cdot x + \frac{1}{N_{min}} \cdot (1 - x) \right] \tag{7}$$

An essential important property of ionic based memristive devices is the back diffusion of the ions. The back diffusion determines the reliability and the storage time of the memristive device and is crucial parameter for a precise adjustment of multiple resistance states. In order to consider this behavior in the model, a further term was added to **Eq. 6**:

$$c_{drift} = \frac{\mu_n \cdot R_{mean}}{d_{HfOx} \cdot A} - c_{back} \cdot \left[1 - (2x - 1)^2\right] \tag{8}$$

Here c_{back} is a parameter that describes the strength of the back diffusion and must be adapted to the measured data.

The ion current can be written in the following form using the law of Mott and Gurney (Hardtdegen et al., 2018):

$$I_{Ion} = 4AeN_{mean}a\nu_0 \cdot \exp\left(-\frac{\Delta W}{V_T}\right) \cdot \sinh\left(\frac{a \cdot E_{HfOx}}{V_T}\right) \tag{9}$$

where ΔW is the diffusion barrier, which is reduced by the electric field E_{HfOx}. Furthermore, V_T is the thermal voltage, a the hopping distance, and ν_0 is the attempt frequency. N_{mean} determines the mean concentration of mobile ion species in the HfO_x layer, i.e., $N_{mean} = \frac{1}{2} \cdot (N_{max} + N_{min})$, while A is the active area of the device, which depends on the device type (cf. **Figure 2B**). Thus $A = A_{fil}$ for the filamentary device and $A = A_{device}$ for the interface based switching device (cf. **Figure 2B**).

The interface between the HfO_x/Au is assumed to be the relevant interface for the resistive switching process in both types of devices. In the simulation, this interface is modeled as a Schottky diode with variable Schottky barrier (ϕ_B). Using the thermionic emission theory, the charge transport over a Schottky barrier can be described in the following equation (Sze and Ng, 2006):

$$I_S = I_R\left(\exp^{\frac{eV}{nV_T}} - 1\right) \tag{10}$$

Where n is the ideality factor, which describes the deviation from an ideal diode characteristic, and I_R the reverse current, which is given by:

$$I_R = A^* A T^2 \cdot \exp^{\frac{-e\phi_B}{V_T}} \tag{11}$$

where A^* is the effective Richardson constant, which is $1.20173 \cdot 10^6 Am^{-2}K^{-2}$, T the local temperature, and A the active area. Under negative voltage polarities, however, the reverse current decreases gradually with the applied bias voltage. Therefore, on this polarity the reverse current is (Sze and Ng, 2006):

$$I_{R,v<0} = -A^* A T^2 \cdot \exp^{\frac{-e\phi_B}{V_T}} \exp^{\frac{-e\alpha_r\sqrt{|V|}}{V_T}} \tag{12}$$

Here α_r is a device dependent parameter. In our model we assumed that both quantities n and ϕ_B depend on the concentration of moved ions at the Au/HfO_x interface. A higher concentration of the negatively charged oxygen ions at that interface in R type devices increases the electron concentration locally. For devices of type F an increased concentration of oxygen vacancies increases the amount of acceptor states for electrons at the interface and thus there is also an accumulation of electrons at the interface. Thus, for both type of devices a reduction of the Schottky barrier is expected, which in turn has a significant effect on the charge transport through the complete device. In the model this was considered by a state variable dependency of those quantities:

$$\phi_B(x) = \phi_B^{LRS} \cdot \frac{x}{x_{max}} + \phi_B^{HRS} \cdot \left(1 - \frac{x}{x_{min}}\right) \tag{13}$$

$$n(x) = n^{LRS} \cdot \frac{x}{x_{max}} + n^{HRS} \cdot \left(1 - \frac{x}{x_{min}}\right) \tag{14}$$

the values for n^{LRS} and n^{HRS}, as well as ϕ_B^{HRS} and ϕ_B^{LRS} were obtained from the experimental I-V curves using **Eq. 10**. Another important parameter influencing the ion movement within the memristive device is the local temperature change. This includes mainly Joule heating and plays a crucial role particularly in filamentary-based device structures. This was taken into account in the simulation model as follows (Ielmini and Milo, 2017).

$$T = I \cdot V \cdot R_{therm} + T_0 \tag{15}$$

Here, R_{therm} is the effective thermal resistance and T_0 is the room temperature. The temperature along the filament is assumed to be relatively homogeneous and thus a uniform filament temperature can be assumed (Ielmini and Milo, 2017).

The device parameters have been carefully collected from measurements and literature and are summarized in **Table 1**. The I-V curves simulated with the model are shown in **Figure 2C** and compared with the measurement curves determined

TABLE 1 | Simulation Parameter.

Parameter	Value		Parameter	Value
	type F	*type R*		
$\Phi_B^{HRS}\,[eV]$	0.25	0.71	$\alpha_r\,[V/A\cdot s]$	$1.2\cdot10^6$
$\Phi_B^{LRS}\,[eV]$	0.06	0.61	$\mu_n\,[m^2/V\cdot s]$	10^{-5}
n^{LRS}	4.5	3.9	$\nu_0\,[Hz]$	$3\cdot10^{11}$
n^{LRS}	5	4.45	ε_r^{TiOx}	17
$N_{max}\,[m^{-3}]$	$2\cdot10^{27}$		ε_r^{HfOx}	5.5
$N_{min}\,[m^{-3}]$	$4\cdot10^{24}$		$\Delta W\,[eV]$	0.425
$N\,[m^{-3}]$		10^{23}	$a\,[nm]$	0.4
$d_{HfOx}\,[nm]$	2–8	2.5	$d_{TiOx}\,[nm]$	30
$j^0_{TiOx}\,[A/m^2]$	$5.8\cdot10^7$	$5.8\cdot10^4$	$R_{therm}\,[K/W]$	$1.1\cdot10^4$
$A_{device}\,[\mu m^2]$		100	$A_{fil}\,[nm^2]$	6,362
C_{back}/C_{drift}	0	$3.25\cdot10^{-11}$	$T_0\,[K]$	273

experimentally. As can be seen from this figure, the model presented here shows very good agreement with the experiment. A more detailed description of the results follows in the next chapter.

3 RESULTS AND DISCUSSION

3.1 Resistive Switching and Statistical Examinations

In **Figure 3A** typical obtained I-V curves of the two kinds of memristive devices (named as F and R) are shown. Common for both device types is that they show bipolar resistive switching with a gradual resistance change. A major difference between both types of devices is their voltage polarity. While type R devices require a positive voltage (applied to the top electrode) to set the device, type F devices require a negative voltage to be applied for the set process. The different polarity behaviors are originated from differences in concentration and species of mobile ions, which will be discussed in *Concentration of Mobile Icon*. Furthermore, while a highly rectifying memristive behavior is observed for device type R, a more symmetric memristive behavior is found for devices of type F together with a 3 times higher current level as compared to type R devices (cf. **Figure 3A**). In some more detail: the rectifying

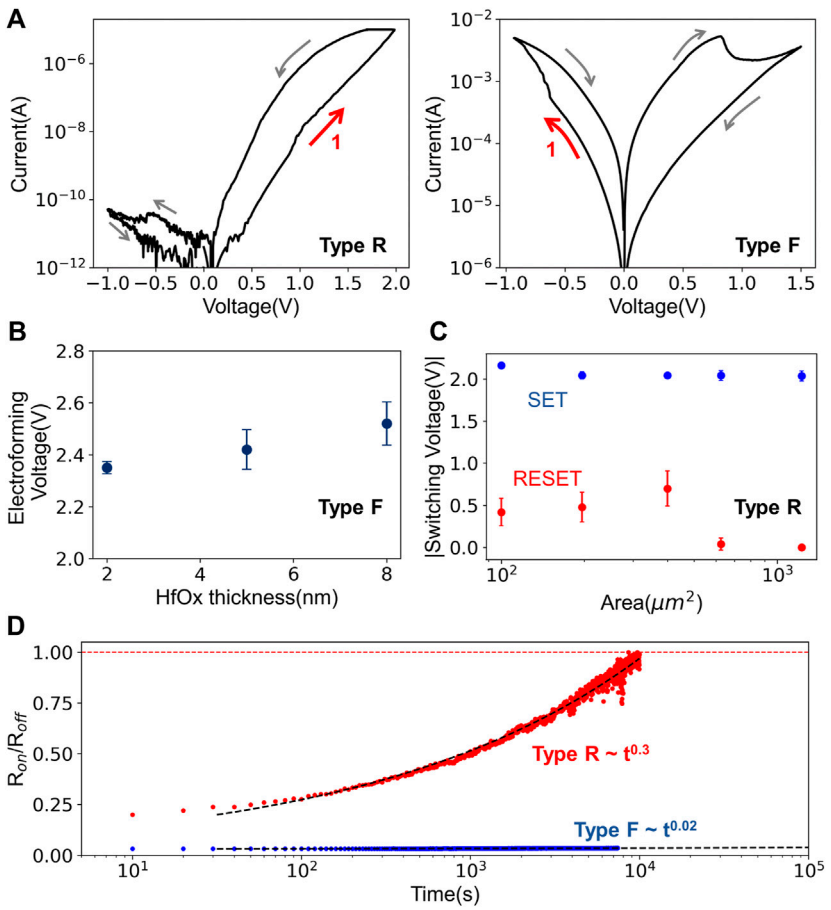

FIGURE 3 | (A) Representative I-V curves of TiN/TiO_x/HfO_x/Au bi-layer memristive devices for type R **(left)**, and type F **(right)**. The arrows point to the resistive switching direction. A clear rectifying behavior was observed in the type R, and a symmetric switching behavior in the type F. **(B)** Electroforming voltage (median values) as a function of HfO_x thickness. Electroforming voltages were tailored by the thickness of the HfO_x in type F. **(C)** SET (blue) and RESET (red) voltages (median values) as a function of device active area size. The smaller the area is, the lower SET/RESET voltage was observed. **(D)** Retention measurement and fitting curves. Type F devices (blue) showed an improved retention characteristic compared to type R (red). The fitted curves are shown with dashed lines, and the fitting constants were 0.02 and 0.3 for type F and type R, respectively.

behavior of devices of type R can be quantified by the ratio between the maximum and minimum current $r_{asym} = |I_{max}/I_{min}|$ at a voltage of ±0.5 V. Here we were able to determine $r_{asym} = 70$ for an active device area of 100 μm^2 which, however, has a strong area dependence. In particular, for an area of 625 μm^2 the asymmetry ratio r_{asym} is reduced from 70 to 4 (further information is provided in **Supplementary Figure 3**).

An important property of memristive devices and another difference between the here considered devices is the initial electroforming process. While no initial electroforming step was necessary for type R devices, type F devices had to be electroformed at the beginning. For a more precise discussion of the electroforming process of type F devices, the median of the required voltages as a function of the thickness of the HfO_x layer is depicted in **Figure 3B**. In detail, electroforming voltages of 2.35, 2.42, and 2.52 V have been observed for, respectively, a 2, 5, and 8 nm thick HfO_x layer. Thus, the electroforming voltage shows moderate thickness scalability. After the electroforming process type F device are operated typically at a maximum (minimum) voltage ±0.75 V. In terms of operating voltage, type F devices also differed from type R devices: type R devices require on average a 1.3 V higher operating voltage with a moderate area dependence (cf. **Figure 3C**). The operating voltages for type R devices were 2.2 V/−0.42 V (SET/RESET) for the smallest area size and 1.7V/0 V for the largest area size. However, the type R devices show a more gradual transition from the inertial high resistive state (HRS) to the low resistive state (LRS) (cf. **Figure 3A**).

A crucial property of memristive devices is their retention time. Furthermore, a detailed investigation of the retention characteristic already provides important conclusions about the underlying resistive switching mechanism (Hansen et al., 2015). The retention behavior for the here discussed two types of memristive bi-layer structures are shown in **Figure 3D**. For the measurement of the retention characteristics, the two types of devices were initially set to the low resistance state and then the resistance value of the devices was determined at regular intervals by means of voltage pulses. As can be seen in the figure, the two types of devices show quite different retention behaviors. For device type R, diffusive characteristics were observed (see red data points in **Figure 3D**), while much higher retention is observed for device type F. In order to analyze the retention characteristics in some more detail the retention curves were fitted using a power law according to the Curie-von Schweidler equation (Mikheev et al., 2014; Goossens et al., 2018):

$$R = R_{on}/R_{off} \propto t^{\alpha} \tag{16}$$

where α is a fit parameter, which is between 0 and 1 (Yang et al., 2010). As a result, $\alpha = 0.3$ is observed for devices of type R, whereas $\alpha = 0.02$ best reflects the experimental data for devices of type F. While $\alpha = 0.02$ describes a very good retention time for devices of type F, $\alpha = 0.3$ shows clearly lower retention for devices of type R. This difference can be explained by the different ion dynamics between the two devices. While in the type R device the filamentary structures are suppressed and mobile oxygen ions are shifted toward the electrode, in the type F devices oxygen vacancies are organized in filamentary structures. This leads to different activation energies of the ion dynamics. It has been shown that the activation energy of oxygen vacancies is in the range of 6–8 eV inside filaments (McKenna, 2014), while it is less than 1 eV outside filaments (Dirkmann et al., 2016; Dirkmann et al., 2018). Furthermore, it is worth mentioning that localized electronic states at the Au/HfOx interface can also contribute to the observed switching mechanism. The localized electronic states are filled or emptied depending on the applied bias voltage polarity (Hansen et al., 2015; Zhou et al., 2016). Even if the exact mechanism underlying the switching effect cannot be clearly explained by the presented measurements alone, the strong difference in the retention times and the different voltage polarity indicate that oxygen vacancies dominate the respective switching behavior in type F devices, while mobile oxygen ions lead to resistive switching in type R devices.

In order to be able to make suitable statements about possible applications of the memristive devices in neuromorphic systems and to tailor the device characteristics accordingly, a statistical investigation of relevant device parameters is required. As relevant device parameters we considered the thickness of the active HfO_x layer (d_{HfOx}), the active area size A, and the concentration of mobile ions N. The results of that investigation are shown in **Figure 4**. In the cumulative distribution function (CDF) of the resistance of type R devices (**Figure 4A**) and of type F devices (**Figure 4B**) the resistances were obtained from voltage sweep measurements by calculating the corresponding median values and the standard deviations. The resistance obeyed a lognormal distribution for all examined devices. For devices of type R (cf. **Figure 4A**) the resistance distributions for area sizes from 100 to 1,225 μm^2 are shown. For the devices of type F the different curves in **Figure 4B** originate from the different d_{HfOx}. As a result, we found that for devices of type R the resistance window decreased with increasing active area size A which can be attributed to the decreasing rectifying ratio (further details are in the supplement). Furthermore, the relatively small width of the CDF curve was observed for type R devices indicating a high device uniformity. For the devices of type F, the low resistant states show a steeper change in the CDF curve than the high resistant states. Even though the found variations in the resistances are small, the devices with a HfO_x thickness of 5 nm show here the best variability.

To be able to make detailed statements about the requirements to be met by the physical device parameters, the influence of the variability in relation to the physical parameters must be examined. Therefore, normalized standard deviations of the devices were determined and plotted as a function of the active volume, i.e., the layer thickness of the active HfO_x layer times the device area. The obtained results for both types of devices are shown in **Figure 4C**. The figure shows the different measured variabilities for the devices of type R (triangular data points) and the devices of type F (circular data points) as a function of the active volume of the device. For devices of type R it appears that the variability is only weakly affected by increased area size. Here the normalized standard deviation of 0.2 is quite constant over the investigated area sizes (see the dashed black line in **Figure 4C**). However, for devices of type F a parabolic curve best describes the found trend which indicates a clear optimum at

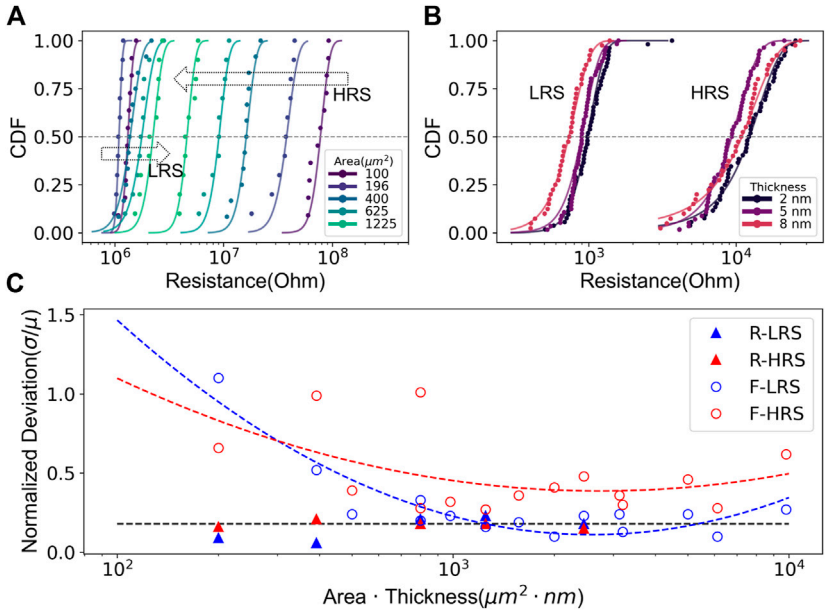

FIGURE 4 | Resistance distribution for different physical device parameters in type R devices **(A)**, and type F devices **(B)**. **(A)** CDF for different active device area sizes of device type R. The arrows point to the direction of the increasing area. **(B)** CDF for different HfO_x thicknesses in type F devices. **(C)** Device variability (σ/μ) in terms of physical device parameters. The variability of type R devices is marked with triangles, and type F devices with circles. Red color for high resistance states, and blue color for the low resistance were used. The fitted curves are shown with dashed lines. For type F devices a parabolic trend was observed, which shows a correlation between the area and the thickness of the HfO_x in the variability of devices.

approximately $2.6 \cdot 10^3\ \mu m^2 \cdot nm$ for the HRS and $2.73 \cdot 10^3\ \mu m^2 \cdot nm$ for the LRS. This means that a reduction from $d_{HfOx} = 8\ nm$ to $d_{HfOx} = 2\ nm$ increases the optimal device area from $A_{device} = (18 \times 18)\ \mu m^2$ to $A_{device} = (36 \times 36)\ \mu m^2$. Thus, the trend can be observed that with extremely small layer thicknesses, a larger area leads to a more stable device behavior.

3.2 Resistive Switching Mechanism and Device Requirements

A sound understanding of the resistive switching mechanism is important to enable a targeted design of the memristive devices for application in neuromorphic systems. For this reason, the device model described in *Physics Based Device Model* was used to interpret the experimental results described above. The obtained results are shown in **Figure 2C**. Therein the experimental I-V curves are compared with simulated curves. The used simulation parameters are summarized in **Table 1**. In both cases, i.e., in the case of the filamentary (type F device) and the interface-based device (type R device), one can see quite good agreement between simulation model and experiment. The main difference between the two I-V curves in the simulation model comes from (i) differences in concentration and species of mobile ions due to stoichiometric differences between Hf and O, (ii) different active areas that are responsible for the switching behavior (cf. **Figure 2C**), and (iii) the lowering of the Schottky barrier and the change of the ideality factor. In order to understand more exactly the underlying switching mechanisms that lead to the different device characteristics, the mentioned points (i–iii) will be discussed in the following in more detail.

3.2.1 Schottky Barrier Height Lowering

From the measured I-V curves the minimum and the maximum values of the variation of the Schottky barrier were determined. Therefore, **Eq. 11** was adapted to the experimental data at the voltage interval ranging from 0 to 100 mV for both device types. Furthermore, we made the assumption that the resistance of the device does not change in that interval. As a result, we found that the values for the Schottky barriers vary between 65 meV and 250 meV for the filamentary device F (upper graph in **Figure 2C**), whereby a barrier variation of 615 meV and 708 meV was obtained for the area-based device R (lower graph in **Figure 2C**). In addition, the fit procedure also considered the ideality factor as an adjustable parameter, whereby we obtained 5.0 and 4.54 for filamentary device F and 3.9 and 4.45 for the area-based device R. A key finding from that analysis is that area-based device has a much higher Schottky barrier, while for both devices a strong variation of the Schottky barrier is observed. In order to analyze that finding in more detail, simulations were carried out with a maximal barrier lowering of 200 meV. The results of the simulations for the two device types are shown in **Figure 5**. The obtained changes in the resistance value for the type R (**Figure 5A**) and type F devices (**Figure 5B**) are shown. For this purpose, the Schottky barrier of the high ohmic state (see indicated ϕ_B^{HRS} in the figures) was used as a starting value and the barrier height was successively reduced, i.e., $\Delta\phi_B = (\phi_B^{HRS} - \phi_B^{LRS})$. This confirms the experimentally observed finding of a strong

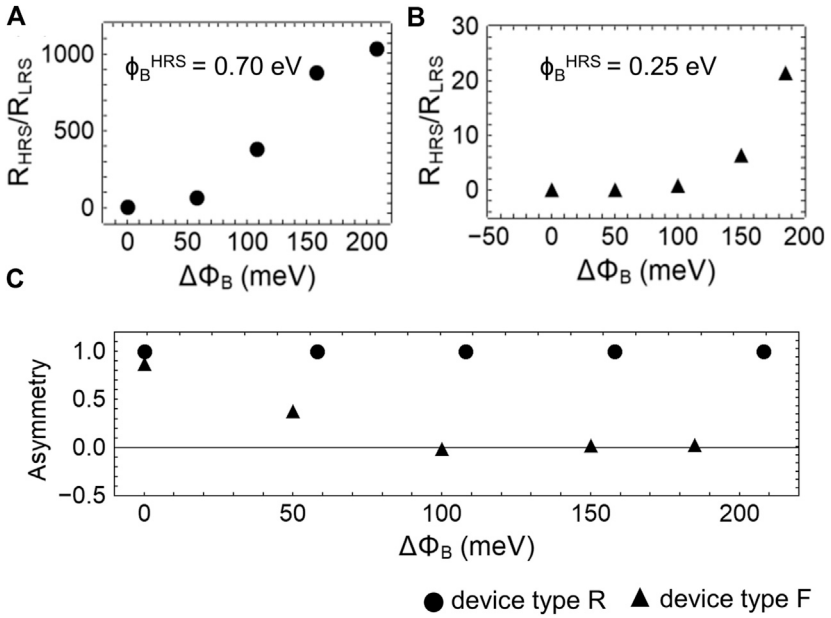

FIGURE 5 | Influence of the Schottky barrier height lowering $\Delta\Phi_B$ on the device resistance: the resistance value as a function of Schottky barrier lowering for type R devices **(A)** and type F devices **(B)**. Φ_B^{HRS} is the inertial Schottky barrier height for the respective R and F type device. **(C)** Asymmetry as a function of the barrier lowering. Strong asymmetric characteristics are observed in device R (circle) within 200 *meV* in the barrier lowering, while the asymmetry was destroyed in device F (triangles) at 100 *meV* barrier lowering.

dependence of the resistance change of the devices on the maximum barrier lowering for both types of devices. Two types showed different switching mechanisms: filamentary- and interface-type. However, Schottky contact adjustment was an essential factor in resistive switching behaviors for both typem F and type R devices. Thus, it can be stated that the Schottky barrier change is the main reason for the switching behavior of the two different memristive devices, which is in good agreement with previously published data (Hansen et al., 2015; Hardtdegen et al., 2018).

In fact, a significant influence on the Schottky barrier height and therewith an important technology parameter is the material used for the electrode and the oxide layer. Since the same electrode material (Au) was used for both types of devices, the observed difference can only come from the HfO_x layer. In this respect, the difference is mainly in the layer quality due to the different manufacturing processes that we used for the two devices. This has a particular effect on the number of oxygen ions and vacancies, which we will discuss in more detail below. However, a qualitative indicator of contact quality is the asymmetry between the minimum and the maximum current values in the I-V characteristics and the ideality factor n of the contacts. Here we observe that n is lower for the type R devices than for the type F devices and the type R devices show a clear asymmetry and therefore a stronger rectifying characteristic. To investigate this point, the asymmetry as a function of the barrier lowering $\Delta\phi_B$ is shown in **Figure 5C**. The asymmetry was determined by the following formula: $[(I_{max} - I_{min})/(I_{max} + I_{min})]$. As a result, we found that the barrier lowering of the area-based devices does not affect the asymmetry, whereas 100 mV of the type F devices is sufficient to completely destroy the asymmetry.

3.2.2 Concentration of Mobile Ions

One of the most important parameters for the resistance switching mechanism of memristive devices is the concentration of mobile ions. In the simulation model we have, therefore, investigated the concentration of mobile ions in the HfO_x layer as a further central device parameter. It turned out that for the rectifying device R a constant low concentration of negatively charged oxygen ions ($N_{min} = N_{max} = 10^{23}\ m^{-3}$) best describes the experimental I-V curve, where a variation of positively charged oxygen vacancies from $N_{min} = 4 \cdot 10^{24}\ m^{-3}$ to $N_{max} = 2 \cdot 10^{27}\ m^{-3}$ for the filamentary device F gives the best agreement with the experiment (cf. **Figure 2C**). These obtained results are in good agreement with previous investigations (Dirkmann et al., 2016; Hardtdegen et al., 2018) and support the model outlined in **Figure 2A**. In order to investigate these variations, the concentration of oxygen vacancies was varied in the range from $5.2 \cdot 10^{25}\ m^{-3}$ to $2.5 \cdot 10^{27}\ m^{-3}$ for F type device and a variation from $1 \cdot 10^{22}\ m^{-3}$ to $1 \cdot 10^{24}\ m^{-3}$ of oxygen ions were used for the rectifying device type R. The simulation results are summarized in **Figure 6**.

Figure 6A shows I-V curves for the filamentary device with different mean concentrations of oxygen vacancies. In particular, two major trends for the change in oxygen vacancies can be seen: (i) the hysteresis shows a clear variation with the change of the oxygen vacancies, and (ii) the values for set and reset voltages become smaller. To interpret these two properties in more detail, **Figure 6B** shows the ratio R_{HRS}/R_{LRS} at −0.1 V as a function of the

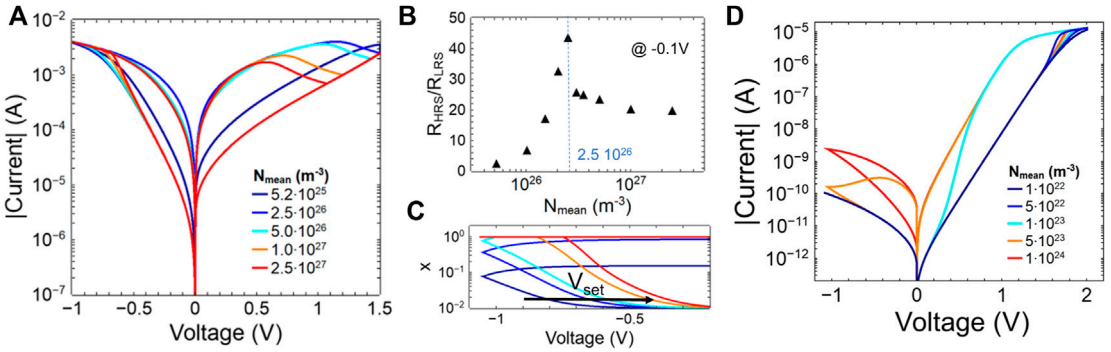

FIGURE 6 | Simulated I-V curves of TiN/TiO_x/HfO_x/Au bi-layer memristive devices with a variation of the mean concentration of mobile ions in the HfO_x layer. **(A)** The variation of the mean concentration of positively charged ions in the range from $5.2 \cdot 10^{25}\ m^{-3}$ to $2.5 \cdot 10^{27}\ m^{-3}$ is simulated for type F. **(B)** The ratio of R_{HRS}/R_{LRS} at −0.1 V as a function of the mobile ions. The optimum memristive hysteresis was observed at the mobile ion concentrations of $2.5 \cdot 10^{26}\ m^{-3}$. **(C)** The state variable (x) as a function of the applied voltages for different concentrations of mobile ions in the HfO_x layer. Operating voltages (SET/RESET voltage and threshold voltage) in the bi-layer memristive devices were affected by the concentration of mobile ions in the HfO_x layer. **(D)** The variation of the concentration of negatively charged ions in the range from $1 \cdot 10^{22}\ m^{-3}$ to $1 \cdot 10^{24}\ m^{-3}$ is simulated for type R. The resistance values and the hysteretic effects were influenced by the concentration of oxygen ions.

concentration of oxygen vacancies. What can be seen very clearly is that there is an optimum of the ratio at $2.5 \cdot 10^{26}\ m^{-3}$. The reason for this is the threshold value of the oxygen diffusion, which essentially determines R_{HRS} and R_{LRS}. For this purpose, **Figure 6C** shows the state variable x as a function of the applied voltage for the different concentrations at oxygen vacancies. According to **Eq. 7**, the concentration of the oxygen vacancies determines the change of the resistance of the active HfO_x layer, but also the ion drift (see **Eq. 6**), and thus the change of the state variable x. What can be observed from the simulation is that high oxygen vacancy concentrations cause a change in the state variable already at very low voltage values (cf. **Figure 6C**). This means that a threshold value for setting the device can no longer be set precisely, which already leads to a reduced resistance value for a voltage of −0.1 V. However, since threshold values are important for the application, a precise setting of the oxygen vacancies is an important device parameter that should be chosen carefully.

The results for the rectifying memristive device under varying concentrations of oxygen ions are shown in **Figure 6D**. Here it can be seen that the concentration of oxygen ions has an effect on the change of the resistance value as well as on the retention characteristics. Thus, at extremely low concentrations of oxygen ions, only small hysteric effects are observed, while a pronounced hysteresis is only observed at a concentration of $5 \cdot 10^{22}\ m^{-3}$. This concentration of oxygen ions, thus, defines a critical minimum for memristive switching behavior.

3.2.3 Area Dependence

An experimentally important indication of the type of resistive switching mechanism is given by the area dependence of the devices. For this purpose, the product of area times resistance (RA) as a function of the area of the devices is shown for both device types in **Figure 7**. While the upper graph of **Figure 7** is presenting the results from the rectifying device R, the graph on the bottom is showing the area dependency for the filamentary device F. Here, the data points are taken from the measurements

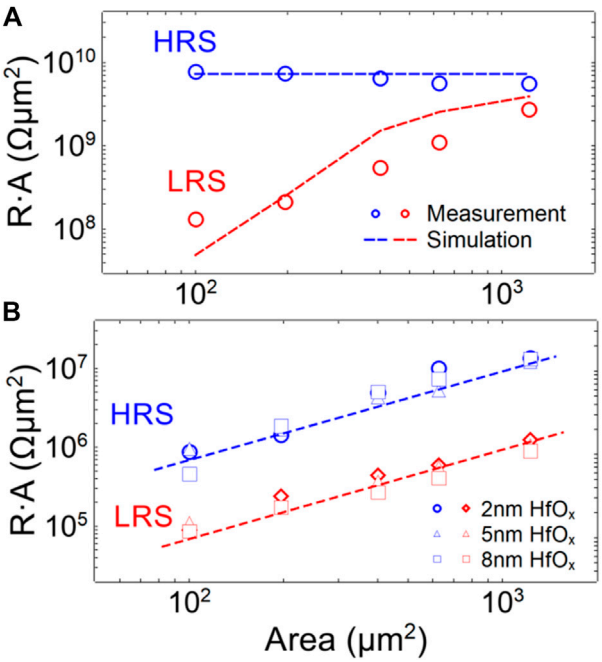

FIGURE 7 | The $R \cdot A$ product as a function of the device active area for **(A)** type R and **(B)** type F. The dashed lines present simulated device models. **(A)** The $R \cdot A$ product showed a constant behavior in HRS for type R, while an area dependent behavior for type F **(B)**. The area dependency of the $R \cdot A$ product in LRS for device R **(A)** was caused by the area dependency of the ion drift constant, which was in good agreement with the simulation results.

and the dashed lines are the results of the simulation model. The expected trend can be seen for the high resistant state of the devices: for the filamentary device F, an area independent behavior is seen, while a clear area dependence was found for the rectifying device R. It is noticeable that the low ohmic state of the rectifying device R shows a non-uniform area dependence.

One would actually expect a horizontal line in the $R \cdot A$ vs. A representation chosen here. This is relevant with the drift constant c_{drift} from **Eq. 8**, which depends on the layer thickness of the HfO_x layer (d_{Hfox}) and the active device area (A). While the changes in the layer thicknesses (d_{Hfox}) in the experimentally investigated interval cause only a small change in c_{drift}, the changes in the area for the rectiyfying device R have a considerable influence on c_{drift}. In this case, the drift constant (c_{drift}) is reduced, especially for large active areas, and thus a smaller change in the state variable x is induced during a voltage ramp. This in turn leads directly to a smaller change in the device resistance, which we can also observe experimentally. Thus, this shows that the choice of the device area has an influence on the dynamics of the oxygen ions and vacancies, especially for the rectifying memristive device. Furthermore, these results give good confirmation of the proposed switching mechanism, i.e., area-based switching for the R-type device and filamentary switching for the F-type device.

3.3 Applications for Neuromorphic Computing

The emulation of synaptic plasticity processes with memristive devices is one of the most important application fields of memristive devices in neuromorphic systems (Ziegler et al., 2018). In particular, this requires the design of suitable learning and training processes (Ielmini and Ambrogio, 2020), which needs a targeted adjustment of the resistance states of individual memristive devices in networks. In the following section, it is presented that type F devices fulfill requirements for machine learning based algorithms, whereas type R devices for neurobiologically inspired learning schemes.

The challenge in the machine learning based algorithm is to create suitable local learning rules that guarantee a local change of the device state so that a requested global network functionality is enabled. Therefore, a general framework is provided by the Hebbian learning rule (Ziegler et al., 2015), which can be systematized in the following equation:

$$\frac{d\omega_{ij}}{dt} = f\left(\omega_{ij}, A_j, A_i\right) \tag{17}$$

where ω_{ij} describes the coupling strength between the pre- and the post-synaptic neuron and $A_{j(i)}$ their activities, as sketched in **Figure 8A**. This formula translates Hebb's postulate, that synaptic connections change only when the respective pre- and post-synaptic neurons are active at the same time. The choice of the function f is thus decisive for the learning or training procedure of any artificial neural network. A common way to realize the weight update according to **Eq. 17** is provided by the delta rule (Kendall et al., 2020), which is at the heart of deep learning neural networks:

$$\Delta\omega_{ij} = \alpha \cdot \left(d_i - y_i\right) \cdot p_j \tag{18}$$

where the coefficient α is named learning rate and is usually positive. Furthermore, p_j is the activity of the pre-neuron (input value), y_i is the activity of the post-neuron (output value), and d_i the desired output value for a given input p_j used during learning. To convert that equation into hardware, the coupling strength ω_{ij} can be represented by the conductance G_{ij} of the memristive device, and y_j, p_j, and d_j by voltage- or current-dependent functions that either increase or decrease the conductance of the memristive device (Linares-Barranco et al., 2011). Thus, for the implementation of memristive devices in neuromorphic network structures via the delta rule a precise change of the conductance in dependence on applied voltage (or current) pulses is required (Payvand et al., 2018).

In order to investigate the resistance update behavior of the devices used here under voltage pulsing, AC pulses trains were used (see the sketch in **Figure 8B**). Therefore, a voltage train of 20 SET pulses followed by 20 RESET pulses was applied to the devices. Furthermore, the resistance states have been determined by a readout pulse that followed each switching pulse. The results obtained are shown in **Figure 8C** for type F devices and in (D) for type R devices. Read pulses of 1.0 and 0.1 V with a pulse width of 10 ms have been used for R and F devices, respectively. For the reset pulse, the width was 1 ms and the amplitudes were −2 and 1.5 V for R and F devices. As a result, a gradual transition change with multiple resistance states was observed in devices of type R, while a more binary behavior was recorded for devices of type F (cf. **Figures 8C,D**). In order to investigate the pulse behavior of the type F devices in more detail with respect to **Eq. 18**, the voltage amplitudes for SET and RESET pulses were successively changed in each pulse, as sketched in the inset of **Figure 8E**. The therewith obtained resistance change as a function of the voltage pulse amplitudes is shown in **Figure 8E**. Thus, a linear change in resistance with a successive incremental increase of the voltage pulse height was recorded for both set and reset. Furthermore, the resistance change was nearly symmetric in both resistance states, presenting 0.44 and 0.56 linearity for set and reset, respectively. Hence, this behavior fulfills nicely the requirement proposed by equation 18 and makes type F devices, together with their relatively good retention, perfect candidates for the hardware realization of deep learning neural networks. In this context, bi-layer oxide memristive devices of similar types have already proven their performance (Yao et al., 2020).

While the delta rule underlies a variety of machine learning systems and allows an effective implementation of Hebb's learning rule within artificial neural networks, there is no explicit time dependence. However, the time dependence of learning processes is an important parameter in biology and determines how the synaptic connection is strengthened or weakened (Panwar et al., 2017). Here, an important property is the memory effect of synapses which leads to a sustained strengthening of the synaptic connection after repeated (high frequency) excitation named long-term potentiation (LTP). Therefore, the respective time interval between the excitation is required. At this respect, the diffusive ionic processes of memristive devices and their memory behavior are unique properties for the emulation of bio-realistic time-dependent learning (Ziegler et al., 2018), such as spike-timing dependent plasticity (STDP) and paired-pulse facilitation (PPF), to only mention two important plasticity processes. Many ways to emulate such learning schemes have been presented in recent years with memristive devices (Wang et al., 2020). However, the

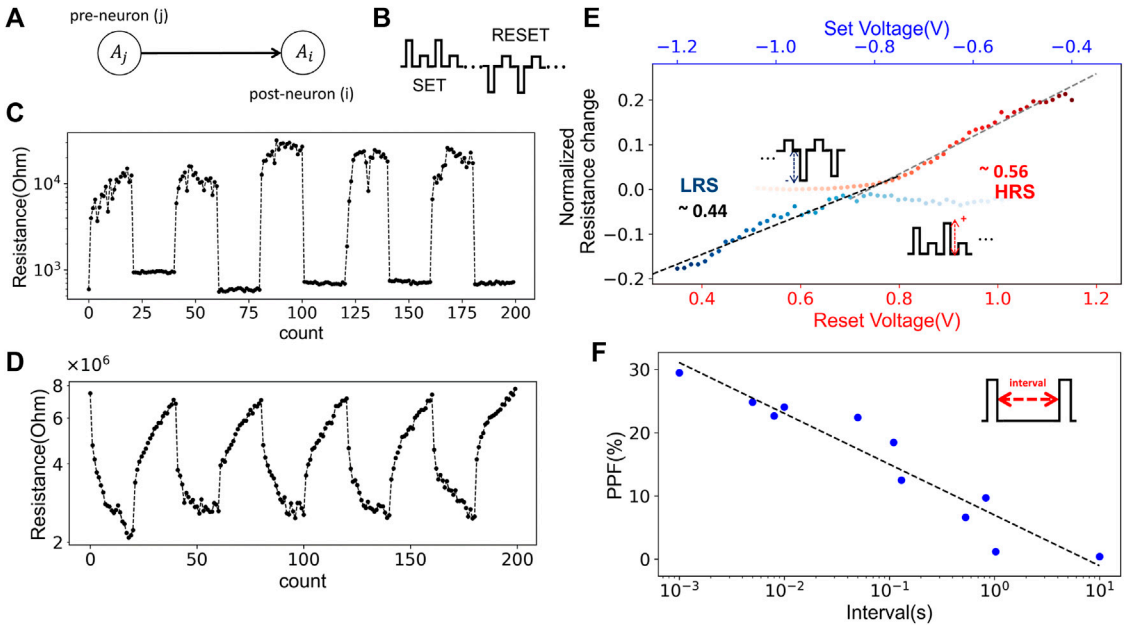

FIGURE 8 | (A) Sketch of synaptic plasticity process. **(B)** The waveform of voltage pulse trains; 20 SET pulses followed by 20 RESET pulses. A readout pulse followed each switching pulse. The resulting change in resistance states under the voltage train is shown in **(C)** for type F, **(D)** for type R. The linearity in resistance change was improved in the type R. **(E)** The resistance as a function of the amplitude of SET/RESET voltages in type F. The amplitude of the applied voltage for a SET (RESET) was decreasing (increasing) to lead a next level in the resistance, and a readout voltage followed each switching voltage pulse. The multistate resistance was observed along with the symmetricity between LRS and HRS. **(F)** PPF as a function of interval time between two sequent switching voltage pulses in type R. The dashed line presents a fitted curve in the experimental data (blue). Increasing the time interval results in the weaker resistance change.

challenge here is to select the correct voltage functions for the pre- and post-neurons, so that an appropriate voltage pulse is applied across the memristive device (Linares-Barranco et al., 2011; Ambrogio et al., 2013). To investigate this for the type R device, we took a closer look at the PPF scheme. The results obtained,therefore, are shown in **Figure 8F**. Two identical sequential SET pulses were applied using different time intervals. In this study, the PPF ratio was defined as the incremental percentage change in the resistance after the first and second pulses. As a result, we found, the longer the time interval is, the smaller the resistance changes with a linear trend. This, particularly, corresponds to the enhanced back diffusion of oxygen ions in R type devices, as discussed above, and resembles well with biology.

4 CONCLUSION

In summary, we have presented two bi-layer TiN/TiO_x/HfO_x/Au memristive devices. Depending on the respective sputtering method, we were able to realize different switching mechanisms. While mobile oxygen ions are responsible for resistance switching in type R devices, oxygen vacancies cause the switching mechanism in type F devices. Using a statistical analysis of the devices and a physical device model, we have investigated the relevant technology and device parameters, and related them to the electronic behavior of the devices. In **Figure 9** these parameters are graphically summarized and their relevance

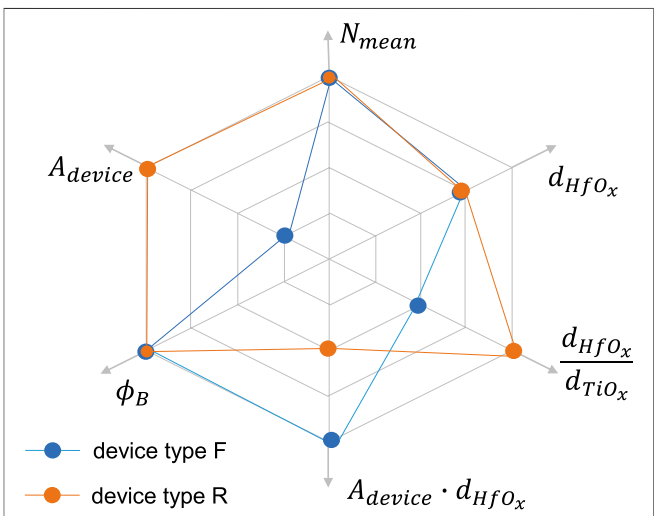

FIGURE 9 | Relevant technology and device parameters to realize a desired resistive switching behavior in the TiN/TiO_x/HfO_x/Au bi-layer memristive devices.

for the respective device type is shown. As you can see from that figure for devices of type R, whose resistive switching is induced by mobile oxygen ions, the device area (A_{device}), the Schottky barrier (ϕ_B), and the ratio d_{HfOx}/d_{TiOx} are important. In devices of type F, whose switching mechanism can be traced back to filamentary oxygen vacancies, also the Schottky barrier (ϕ_B) is

important. But, for that devices the product of A_{device} and d_{HfOx} is more in the focus for good device performance, than A_{device} or d_{HfOx} alone. For both types, however, it is important to adjust the concentration of the mobile charge carriers precisely to reach a reliable performance. In general, it can be concluded that the respective device properties must always be tailored to the specific application. Therefore, we hope that the framework described here helps to identify the relevant technology parameters for that purpose.

DATA AVAILABILITY STATEMENT

The original contributions presented in the study are included in the article/**Supplementary Material**, further inquiries can be directed to the corresponding authors.

AUTHOR CONTRIBUTIONS

SP prepared the samples, JD developed the sputtering technology for the HfOx films, and the characteristics of HfOx films were analyzed using XPS by AK. SP performed the measurements, analyzed the experimental results, and co-wrote the manuscript. SK supervised the electronic measurement. MZ supported the measurements and data interpretation. MZ developed the simulation model. The simulation results were discussed and interpreted between SP, TI, SK, and MZ. TI and MZ conceived the idea, initiated, and supervised the experimental research. SP and MZ discussed the experimental results and contributed to the refinement of the manuscript.

FUNDING

Funded by the Deutsche Forschungsgemeinschaft (DFG, German Research Foundation)–Project-ID 434434223–SFB 1461 and the Carl-Zeiss Foundation via the Project MemWerk.

SUPPLEMENTARY MATERIAL

The Supplementary Material for this article can be found online at: https://www.frontiersin.org/articles/10.3389/fnano.2021.670762/full#supplementary-material.

REFERENCES

Alibart, F., Zamanidoost, E., and Strukov, D. B. (2013). Pattern Classification by Memristive Crossbar Circuits Using *ex situ* and *in situ* Training. *Nat. Commun.* 4, 1–7. doi:10.1038/ncomms3072

Ambrogio, S., Balatti, S., Nardi, F., Facchinetti, S., and Ielmini, D. (2013). Spike-Timing Dependent Plasticity in a Transistor-Selected Resistive Switching Memory. *Nanotechnology* 24, 384012. doi:10.1088/0957-4484/24/38/384012

Asanuma, S., Akoh, H., Yamada, H., and Sawa, A. (2009). Relationship Between Resistive Switching Characteristics and Band Diagrams of Ti/Pr1−xCaxMnO3Junctions. *Phys. Rev. B.* 80, 235113. doi:10.1103/PhysRevB.80.235113

Bousoulas, P., Asenov, P., Karageorgiou, I., Sakellaropoulos, D., Stathopoulos, S., and Tsoukalas, D. (2016). Engineering Amorphous-Crystalline Interfaces in tio2-x/tio2-y-Based Bilayer Structures for Enhanced Resistive Switching and Synaptic Properties. *J. Appl. Phy.* 120, 154501. doi:10.1063/1.4964872

Chandrasekaran, S., Simanjuntak, F. M., Saminathan, R., Panda, D., and Tseng, T. Y. (2019). Improving Linearity by Introducing Al in hfo2 as a Memristor Synapse Device. *Nanotechnology* 30, 445205. doi:10.1088/1361-6528/ab3480

Clima, S., Chen, Y. Y., Chen, C. Y., Goux, L., Govoreanu, B., Degraeve, R., et al. (2016). First-Principles Thermodynamics and Defect Kinetics Guidelines for Engineering a Tailored RRAM Device. *J. Appl. Phy.* 119, 225107. doi:10.1063/1.4953673

Cüppers, F., Menzel, S., Bengel, C., Hardtdegen, A., von Witzleben, M., Böttger, U., et al. (2019). Exploiting the Switching Dynamics of hfo2-Based Reram Devices for Reliable Analog Memristive Behavior. *APL Mater.* 7, 091105. doi:10.1063/1.5108654

del Valle, J., Ramírez, J. G., Rozenberg, M. J., and Schuller, I. K. (2018). Challenges in Materials and Devices for Resistive-Switching-Based Neuromorphic Computing. *J. Appl. Phy.* 124, 211101. doi:10.1063/1.5047800

Diederich, N., Bartsch, T., Kohlstedt, H., and Ziegler, M. (2018). A Memristive Plasticity Model of Voltage-Based stdp Suitable for Recurrent Bidirectional Neural Networks in the Hippocampus. *Sci. Rep.* 8, 1–12. doi:10.1038/s41598-018-27616-6

Dirkmann, S., Hansen, M., Ziegler, M., Kohlstedt, H., and Mussenbrock, T. (2016). The Role of ion Transport Phenomena in Memristive Double Barrier Devices. *Sci. Rep.* 6. 35686. doi:10.1038/srep1375310.1038/srep35686

Dirkmann, S., Kaiser, J., Wenger, C., and Mussenbrock, T. (2018). Filament Growth and Resistive Switching in Hafnium Oxide Memristive Devices. *ACS Appl. Mater. Inter.* 10, 14857–14868. doi:10.1021/acsami.7b19836

Dittmann, R., and Strachan, J. P. (2019). Redox-Based Memristive Devices for new Computing Paradigm. *APL Mater.* 7, 110903. doi:10.1063/1.5129101

Gao, J., He, G., Deng, B., Xiao, D. Q., Liu, M., Jin, P., et al. (2016). Microstructure, Wettability, Optical and Electrical Properties of hfo2 Thin Films: Effect of Oxygen Partial Pressure. *J. Alloy. Compd.* 662, 339–347. doi:10.1016/j.jallcom.2015.12.080

Gao, S., Zeng, F., Li, F., Wang, M., Mao, H., Wang, G., et al. (2015). Forming-Free and Self-Rectifying Resistive Switching of the Simple pt/tao x/N-Si Structure for Access Device-Free High-Density Memory Application. *Nanoscale* 7, 6031–6038. doi:10.1039/c4nr06406b

Goossens, A. S., Das, A., and Banerjee, T. (2018). Electric Field Driven Memristive Behavior at the Schottky Interface of Nb-Doped srtio3. *J. Appl. Phy.* 124, 152102. doi:10.1063/1.5037965

Govoreanu, B., Redolfi, A., Zhang, L., Adelmann, C., Popovici, M., Clima, S., et al. (2013). "Vacancy-Modulated Conductive Oxide Resistive Ram: an Area-Scalable Switching Current, Self-Compliant, Highly Nonlinear and Wide on/off-Window Resistive Switching Cell," in IEEE International Electron Devices Meeting, Washington, DC, December 9–11, 2013 (New York, NY: IEEE), 10–12.

Hansen, M., Zahari, F., Kohlstedt, H., and Ziegler, M. (2018). Unsupervised Hebbian Learning Experimentally Realized With Analogue Memristive Crossbar Arrays. *Sci. Rep.* 8, 1–10. doi:10.1038/s41598-018-27033-9

Hansen, M., Zahari, F., Ziegler, M., and Kohlstedt, H. (2017). Double-Barrier Memristive Devices for Unsupervised Learning and Pattern Recognition. *Front. Neurosci.* 11, 91. doi:10.3389/fnins.2017.00091

Hansen, M., Ziegler, M., and Kolberg, L. (2015). A Double Barrier Memristive Device. *Sci. Rep.* 5, 13753. doi:10.1038/srep13753

Hardtdegen, A., Torre, C. L., Cüppers, F., Menzel, S., Waser, R., and Hoffmann-Eifert, S. (2018). Improved Switching Stability and the Effect of an Internal Series Resistor in hfo2/tiox Bilayer Reram Cells. *IEEE Trans. Electron Devices* 65, 3229–3236. doi:10.1109/TED.2018.2849872

He, W., Sun, H., Zhou, Y., Lu, K., Xue, K., and Miao, X. (2017). Customized Binary and Multi-Level HfO2−x-Based Memristors Tuned by Oxidation Conditions. *Sci. Rep.* 7, 10070. doi:10.1038/s41598-017-09413-9

Huang, C. H., Huang, J. S., Lin, S. M., Chang, W. Y., He, J. H., and Chueh, Y. L. (2012). Zno1−x Nanorod arrays/zno Thin Film Bilayer Structure: From Homojunction Diode and High-Performance Memristor to Complementary 1d1r Application. *Acs Nano* 6, 8407–8414. doi:10.1021/nn303233r

Hur, J. H., Lee, M.-J., Lee, C. B., Kim, Y.-B., and Kim, C.-J. (2010). Modeling for Bipolar Resistive Memory Switching in Transition-Metal Oxides. *Phys. Rev. B* 82, 155321. doi:10.1103/PhysRevB.82.155321

Ielmini, D., and Ambrogio, S. (2020). Emerging Neuromorphic Devices. *Nanotechnology* 31, 092001. doi:10.1088/1361-6528/ab554b

Ielmini, D., and Milo, V. (2017). Physics-Based Modeling Approaches of Resistive Switching Devices for Memory and in-Memory Computing Applications. *J. Comput. Electron* 16, 1121–1143. doi:10.1007/s10825-017-1101-9

Ignatov, M., Ziegler, M., Hansen, M., and Kohlstedt, H. (2017). Memristive Stochastic Plasticity Enables Mimicking of Neural Synchrony: Memristive Circuit Emulates an Optical Illusion. *Sci. Adv.* 3, e1700849. doi:10.1126/sciadv.1700849

Jeong, H., and Shi, L. (2019). Memristor Devices for Neural Networks. *J. Phys. D* 52, 023003. doi:10.1088/1361-6463/aae223

Jiang, Z., Wu, Y., Yu, S., Yang, L., Song, K., Karim, Z., et al. (2016). A Compact Model for Metal–Oxide Resistive Random Access Memory With Experiment Verification. *IEEE Trans. Electron Devices* 63, 1884–1892. doi:10.1109/ted.2016.2545412

Kendall, J. D., Pantone, R. D., and Nino, J. C. (2020). Data From: Deep Learning in Memristive Nanowire Networks. http://arXiv:2003.02642.

Kim, H. J., Zheng, H., Park, J. S., Kim, D. H., Kang, C. J., Jang, J. T., et al. (2017). Artificial Synaptic Characteristics With Strong Analog Memristive Switching in a pt-ceo2-pt Structure. *Nanotechnology* 28, 285203. doi:10.1088/1361-6528/aa712c

Kim, S. G., Han, J. S., Kim, H., Kim, S. Y., and Jang, H. W. (2018). Recent Advances in Memristive Materials for Artificial Synapses. *Adv. Mater. Technol.* 3, 1800457. doi:10.1002/admt.201800457

Krestinskaya, O., James, A. P., and Chua, L. O. (2020). Neuromemristive Circuits for Edge Computing: a Review. *IEEE Trans. Neural Netw. Learn. Syst.* 31, 4–23. doi:10.1109/TNNLS.2019.2899262

Lee, J., Shin, J., Lee, D., Lee, W., Jung, S., Jo, M., et al. (2010). "Diode-Less Nano-Scale zro x/hfo x rram Device With Excellent Switching Uniformity and Reliability for High-Density Cross-Point Memory Applications," in International Electron Devices Meeting. San Francisco, CA. December 6–8, 2010 (New York, NY: IEEE), 19–25.

Lee, J., Park, J., Jung, S., and Hwang, H. (2011). "Scaling Effect of Device Area and Film Thickness on Electrical and Reliability Characteristics of rram," in International Interconnect Technology Conference. Dresden, Germany. May 8–12 , 2011 (New York, NY: IEEE), 1–3.

Legenstein, R. (2015). Nanoscale Connections for Brain-Like Circuits. *Nature* 521, 37–38. doi:10.1038/521037a

Li, J., Zhang, T., Duan, Q., Li, L., Yang, Y., and Huang, R. (2018a). "Engineering Resistive Switching Behavior in Taox Based Memristive Devices for non-von Neuman Computing Applications," in China Semiconductor Technology International Conference. Shanghai, China. March 11–12, 2018 (New York, NY: IEEE), 1–3.

Li, Y., Wang, Z., Midya, R., Xia, Q., and Yang, J. J. (2018b). Review of Memristor Devices in Neuromorphic Computing: Materials Sciences and Device Challenges. *J. Phys. D* 51, 503002. doi:10.1088/1361-6463/aade3f

Li, Y., Fuller, E. J., Sugar, J. D., Yoo, S., Ashby, D. S., Bennett, C. H., et al. (2020). Filament-Free Bulk Resistive Memory Enables Deterministic Analogue Switching. *Adv. Mater.* 32, 2003984. doi:10.1002/adma.202003984

Lin, P., Li, C., Wang, Z., Li, Y., Jiang, H., Song, W., et al. (2020). Three-dimensional Memristor Circuits as Complex Neural Networks. *Nat. Electron.* 3, 225–232. doi:10.1038/s41928-020-0397-9

Linares-Barranco, B., Serrano-Gotarredona, T., Camuñas-Mesa, L. A., Perez-Carrasco, J. A., Zamarreño-Ramos, C., and Masquelier, T. (2011). On Spike-Timing-Dependent-Plasticity, Memristive Devices, and Building A Self-Learning Visual Cortex. *Front. Neurosci.* 5, 26. doi:10.3389/fnins.2011.00026

Ma, H., Feng, J., Lv, H., Gao, T., Xu, X., Luo, Q., et al. (2017). Self-Rectifying Resistive Switching Memory with Ultralow Switching Current in Pt/Ta2O5/HfO2-x/Hf Stack. *Nanoscale Res. Lett.* 12, 1–6. doi:10.1186/s11671-017-1905-3

Martínez, F. L., Toledano-Luque, M., Gandía, J. J., Cárabe, J., Bohne, W., Röhrich, J., et al. (2007). Optical Properties and Structure of hfo2thin Films Grown by High Pressure Reactive Sputtering. *J. Phys. D* 40, 5256. doi:10.1088/0022-3727/40/17/037

Massimiliano, B., and Yuriy, P. (2013). On the Physical Properties of Memristive, Memcapacitive and Meminductive Systems. *Nanotechnology* 24, 7. doi:10.1088/0957-4484/24/25/255201

McKenna, K. P. (2014). Optimal Stoichiometry for Nucleation and Growth of Conductive Filaments in hfox. *Model. Simul. Mater. Sci. Eng.* 22, 025001. doi:10.1088/0965-0393/22/2/025001

Menzel, S., Waters, M., Marchewka, A., Böttger, U., Dittmann, R., and Waser, R. (2011). Origin of the Ultra-Nonlinear Switching Kinetics in Oxide-Based Resistive Switches. *Adv. Funct. Mater.* 21, 4487–4492. doi:10.1002/adfm.201101117

Mikhaylov, A., Belov, A., Korolev, D., Antonov, I., Kotomina, V., Kotina, A., et al. (2020). Multilayer Metal-Oxide Memristive Device with Stabilized Resistive Switching. *Adv. Mater. Technol.* 5, 1900607. doi:10.1002/admt.201900607

Mikheev, E., Hoskins, B. D., and Strukov, D. B. (2014). Resistive Switching and its Suppression in pt/nb:srtio3 Junctions. *Nat. Commun.* 5, 3990. doi:10.1038/ncomms4990

Mohammad, B., Jaoude, M. A., Kumar, V., Al Homouz, D. M., Nahla, H. A., Al-Qutayri, M., et al. (2016). State of the art of Metal Oxide Memristor Devices. *Nanotechno. Rev.* 5, 311–329. doi:10.1515/ntrev-2015-0029

Niu, D., Chen, Y., Xu, C., and Xie, Y. (2010). "Impact of Process Variations on Emerging Memristor". in Proceedings of the 47th Design Automation Conference. San Francisco, CA. July 13–18, 2010 (DAS), (New York, NY: IEEE) 877–882.

Panwar, N., Rajendran, B., and Ganguly, U. (2017). Arbitrary Spike Time Dependent Plasticity in Memristor by Analog Waveform Engineering. *IEEE Electron Device Lett.* 38, 740–743. doi:10.1109/LED.2017.2696023

Park, T. H., Song, S. J., Kim, H. J., Kim, S. G., Chung, S., Kim, B. Y., et al. (2015). Thickness Effect of Ultra-Thin Ta 2 O 5 Resistance Switching Layer in 28 nm-Diameter Memory Cell. *Sci. Rep.* 5, 15965. doi:10.1038/srep15965

Payvand, M., Muller, L. K., and Indiveri, G. (2018). "Event-Based Circuits for Controlling Stochastic Learning with Memristive Devices in Neuromorphic Architectures," in International Symposium on Circuits and Systems. Florence, Italy. May 27–30, 2018 (New York, NY: IEEE), 1–5.

Pei, J.-S., Wright, J. P., Todd, M. D., Masri, S. F., and Gay-Balmaz, F. (2015). Understanding Memristors and Memcapacitors in Engineering Mechanics Applications. *Nonlinear Dyn.* 80, 457–489. doi:10.1007/s11071-014-1882-3

Prezioso, M., Merrikh-Bayat, F., Hoskins, B. D., Adam, G. C., Likharev, K. K., and Strukov, D. B. (2015). Training and Operation of an Integrated Neuromorphic Network Based on Metal-Oxide Memristors. *Nature* 521, 61–64. doi:10.1038/nature14441

Sah, M. P., Kim, H., and Chua, L. (2014). Brains are Made of Memristors. *IEEE Circuits Syst. Mag.* 14, 12–36. doi:10.1109/MCAS.2013.2296414

Snider, G. S. (2008). "Spike-Timing-Dependent Learning in Memristive Nanodevices," in International Symposium on Nanoscale Architectures. Anaheim, CA. June 12–13, 2008 (New York, NY: IEEE), 85–92.

Solan, E., Dirkmann, S., Hansen, M., Schroeder, D., Kohlstedt, H., Ziegler, M., et al. (2017). An Enhanced Lumped Element Electrical Model of a Double Barrier Memristive Device. *J. Phys. D* 50, 195102. doi:10.1088/1361-6463/aa69ae

Stathopoulos, S., Khiat, A., Trapatseli, M., Cortese, S., Serb, A., Valov, I., et al. (2017). Multibit Memory Operation of Metal-Oxide Bi-Layer Memristors. *Sci. Rep.* 7, 17532. doi:10.1038/s41598-017-17785-1

Sun, W., Gao, B., Chi, M., Xia, Q., Yang, J. J., Qian, H., et al. (2019). Understanding Memristive Switching via in Situ Characterization and Device Modeling. *Nat. Commun.* 10, 1–13. doi:10.1038/s41467-019-11411-6

Sze, S., and Ng, K. K. (2006). *Physics of Semiconductor Devices*. Hoboken, New Jersey: John Wiley & Sons, Ltd.

Tsuruoka, T., Terabe, K., Hasegawa, T., Valov, I., Waser, R., and Aono, M. (2012). Effects of Moisture on the Switching Characteristics of Oxide-Based, Gapless-Type Atomic Switches. *Adv. Funct. Mater.* 22 70–77. doi:10.1002/adfm.201101846

Versace, M., and Chandler, B. (2010). The Brain of a new Machine. *IEEE Spectr.* 47, 30–37. doi:10.1109/MSPEC.2010.5644776

Wang, C., Xiong, L., Sun, J., and Yao, W. (2019). Memristor-Based Neural Networks With Weight Simultaneous Perturbation Training. *Nonlinear Dyn.* 95, 2893–2906. doi:10.1007/s11071-018-4730-z

Wang, M., Luo, W. J., Wang, Y. L., Yang, L. M., Zhu, W., Zhou, P., et al. (2010). "A Novel Cuxsiyo Resistive Memory in Logic Technology with Excellent Data Retention and Resistance Distribution for Embedded Applications," in Symposium on VLSI Technology. Honolulu, HI. June 15–17, 2010 (New York, NY: IEEE), 89–90.

Wang, R., Yang, J.-Q., Mao, J.-Y., Wang, Z.-P., Wu, S., Zhou, M., et al. (2020). Recent Advances of Volatile Memristors: Devices, Mechanisms,

and Applications. *Adv. Intell. Sys.* 2, 2000055. doi:10.1002/aisy.202000055

Wang, Y.-F., Lin, Y.-C., Wang, I.-T., Lin, T.-P., and Hou, T.-H. (2015). Characterization and Modeling of Nonfilamentary Ta/TaOx/TiO2/Ti Analog Synaptic Device. *Sci. Rep.* 5, 10150. doi:10.1038/srep10150

Wang, Z., Yin, M., Zhang, T., Cai, Y., Wang, Y., Yang, Y., et al. (2016). Engineering Incremental Resistive Switching in Taoxbased Memristors for Brain-Inspired Computing. *Nanoscale* 8, 14015–14022. doi:10.1039/C6NR00476H

Xiong, W., Zhu, L. Q., Ye, C., Yu, F., Ren, Z. Y., and Ge, Z. Y. (2019). Bilayered Oxide-Based Cognitive Memristor with Brain-Inspired Learning Activities. *Adv. Electron. Mater.* 5, 1900439. doi:10.1002/aelm.20190043

Yakopcic, C., Hasan, R., and Taha, T. M. (2015). "Memristor Based Neuromorphic Circuit for *ex-situ* Training of Multi-Layer Neural Network Algorithms," in International Joint Conference on Neural Networks. July 12–17, 2015 (New York, NY: IEEE), 1–7.

Yang, C.-H., Kuo, Y., and Lin, C.-H. (2010). Charge Detrapping and Dielectric Breakdown of Nanocrystalline Zinc Oxide Embedded Zirconium-Doped Hafnium Oxide High-K Dielectrics for Nonvolatile Memories. *Appl. Phys. Lett.* 96, 192106. doi:10.1063/1.3429590

Yao, P., Huaqiang, W., Wu, H., Tang, J., Zhang, Q., Zhang, W., et al. (2020). Fully Hardware-Implemented Memristor Convolutional Neural Network. *Nature* 577, 641–646. doi:10.1038/s41586-020-1942-4

Yin, X.-B., Tan, Z.-H., and Guo, X. (2015). The Role of Schottky Barrier in the Resistive Switching of SrTiO3: Direct Experimental Evidence. *Phys. Chem. Chem. Phys.* 17, 134–137. doi:10.1039/c4cp04151h

Yoon, J. H., Song, S. J., Yoo, I.-H., Seok, J. Y., Yoon, K. J., Kwon, D. E., et al. (2014). Highly Uniform, Electroforming-Free, and Self-Rectifying Resistive Memory in the pt/ta2o5/hfo2-x/tin Structure. *Adv. Funct. Mater.* 24, 5086–5095. doi:10.1002/adfm.201400064

Zhao, M., Gao, B., Tang, J., Qian, H., and Wu, H. (2020). Reliability of Analog Resistive Switching Memory for Neuromorphic Computing. *Appl. Phy. Rev.* 7, 011301. doi:10.1063/1.5124915

Zhou, G., Duan, S., Li, P., Sun, B., Wu, B., Yao, Y., et al. (2018). Coexistence of Negative Differential Resistance and Resistive Switching Memory at Room Temperature in Tio x Modulated by Moisture. *Adv. Electron. Mater.* 4, 1700567. doi:10.1002/aelm.201700567

Zhou, G., Ren, Z., Sun, B., Wu, J., Zou, Z., Zheng, S., et al. (2020). Capacitive Effect: an Original of the Resistive Switching Memory. *Nano Energy* 68, 104386. doi:10.1016/j.nanoen.2019.104386

Zhou, G., Sun, B., Yao, Y., Zhang, H., Zhou, A., Alameh, K., et al. (2016). Investigation of the Behaviour of Electronic Resistive Switching Memory Based on Mose2-Doped Ultralong se Microwires. *Appl. Phys. Lett.* 109, 143904. doi:10.1063/1.4962655

Ziegler, M., Riggert, C., Hansen, M., Bartsch, T., and Kohlstedt, H. (2015). Memristive Hebbian Plasticity Model: Device Requirements for the Emulation of Hebbian Plasticity Based on Memristive Devices. *IEEE Trans. Biomed. Circuits Syst.* 9, 197–206. doi:10.1109/tbcas.2015.2410811

Ziegler, M., Wenger, C., Chicca, E., and Kohlstedt, H. (2018). Tutorial: Concepts for Closely Mimicking Biological Learning With Memristive Devices: Principles to Emulate Cellular Forms of Learning. *J. Appl. Phy.* 124, 152003. doi:10.1063/1.5042040

Conflict of Interest: The authors declare that the research was conducted in the absence of any commercial or financial relationships that could be construed as a potential conflict of interest.